Angewandte Chemie
Eine Zeitschrift der Gesellschaft Deutscher Chemiker

Supporting Information

# Quantum Interference in Mixed-Valence Complexes: Tuning Electronic Coupling Through Substituent Effects

*D. P. Harrison, R. Grotjahn, M. Naher, S. M. B. H. Ghazvini, D. M. Mazzucato, M. Korb, S. A. Moggach, C. Lambert, M. Kaupp*, P. J. Low**

**Table S1.** Selected bond lengths from optimized structures of [**5**´] – [**8**´]. [**5**´]$^+$ – [**8**´]$^+$ and [**5a**´]$^+$ – [**8a**´]$^+$.[a]

| | [**5**´] | [**5**´]$^+$ | [**5a**´]$^+$ | [**6**´] | [**6**´]$^+$ | [**6a**´]$^+$ | [**7**´] | [**7**´]$^+$ | [**7a**´]$^+$ | [**8**´] | [**8**´]$^+$ | [**8a**´]$^+$ |
|---|---|---|---|---|---|---|---|---|---|---|---|---|
| P11-Ru(1) | 2.273 | 2.321 | 2.305 | 2.288 | 2.320 | 2.302 | 2.272 | 2.326 | 2.295 | 2.274 | 2.305 | 2.295 |
| P12-Ru(1) | 2.264 | 2.306 | 2.292 | 2.268 | 2.309 | 2.291 | 2.272 | 2.311 | 2.290 | 2.269 | 2.304 | 2.283 |
| Ru(1)-Cα | 1.978 | 1.911 | 1.921 | 1.973 | 1.910 | 1.921 | 1.979 | 1.916 | 1.918 | 1.982 | 1.914 | 1.920 |
| Cα≡Cβ(1) | 1.235 | 1.248 | 1.248 | 1.234 | 1.248 | 1.247 | 1.235 | 1.248 | 1.247 | 1.234 | 1.250 | 1.250 |
| Cβ≡Cα (2) | 1.235 | 1.237 | 1.238 | 1.234 | 1.235 | 1.238 | 1.235 | 1.238 | 1.237 | 1.233 | 1.237 | 1.238 |
| Cα-Ru(2) | 1.983 | 1.970 | 1.970 | 1.976 | 1.965 | 1.971 | 1.980 | 1.971 | 1.974 | 1.971 | 1.960 | 1.963 |
| Ru(2)-P21 | 2.273 | 2.279 | 2.271 | 2.276 | 2.277 | 2.269 | 2.273 | 2.279 | 2.265 | 2.285 | 2.287 | 2.274 |
| Ru(2)-P22 | 2.270 | 2.266 | 2.263 | 2.268 | 2.265 | 2.260 | 2.270 | 2.269 | 2.265 | 2.267 | 2.270 | 2.266 |

[a] LH20t-D3(BJ)/def2-SVP, COSMO($CH_2Cl_2$).

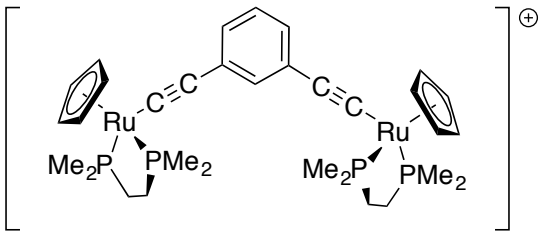


[**5a'**]$^+$

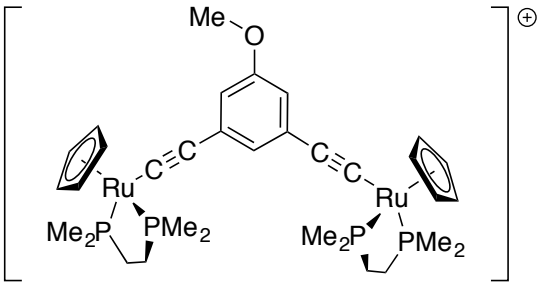


[**6a'**]$^+$

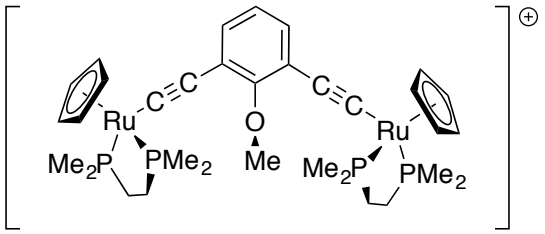


[**7a'**]$^+$

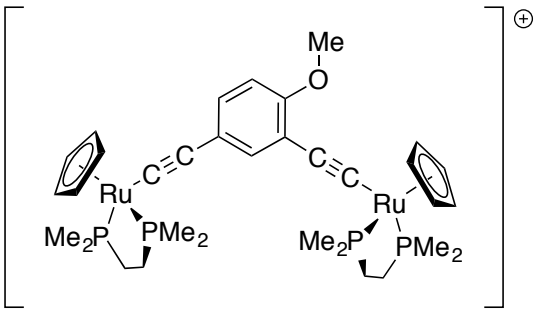


[**8a'**]$^+$

**Scheme S1.** The simplified model mixed-valence complexes [**5a**´]$^+$ – [**8a**´]$^+$.

**Table S2**. Summary of the composition (%) of the β-HOSO and β-LUSO and TDDFT calculated energy ($cm^{-1}$) and oscillator strength ($f_{osc}$) of the β-HOSO and β-LUSO (IVCT) transition of the systems [**5**˙]$^+$ – [**8**˙]$^+$ and [**5a**˙]$^+$ – [**8a**˙]$^+$.[a]

| | | Ru(1) | $C_\alpha C_\beta(1)$ | $C_6H_n$ | OMe | $C_\alpha C_\beta(2)$ | Ru(2) | β-HOSO → β-LUSO ($f_{osc}$) |
|---|---|---|---|---|---|---|---|---|
| [**5**˙]$^+$ | β-LUSO | 36.6 | 26.8 | 17.3 | - | 0.4 | 0.3 | 3548 |
| | β-HOSO | 0.9 | 0.5 | 13.6 | - | 25.0 | 38.3 | (0.0174) |
| [**5a**˙]$^+$ | β-LUSO | 38.7 | 26.0 | 17.7 | - | 0.2 | 0.2 | 3871 |
| | β-HOSO | 0.7 | 0.4 | 13.0 | - | 24.4 | 41.5 | (0.0143) |
| [**6**˙]$^+$ | β-LUSO | 36.3 | 27.2 | 18.3 | 0.2 | 0.2 | 0.1 | 3217 |
| | β-HOSO | 0.4 | 0.3 | 13.4 | 0.0 | 25.4 | 38.7 | (0.0066) |
| [**6a**˙]$^+$ | β-LUSO | 39.3 | 25.9 | 17.0 | 0.1 | 0.1 | 0.1 | 3656 |
| | β-HOSO | 0.4 | 0.3 | 14.2 | 0.1 | 24.4 | 41.1 | (0.0069) |
| [**7**˙]$^+$ | β-LUSO | 37.9 | 26.5 | 17.3 | 0.8 | 0.1 | 0.1 | 4169 |
| | β-HOSO | 0.3 | 0.2 | 10.6 | 0.8 | 24.7 | 39.9 | (0.0060) |
| [**7a**˙]$^+$ | β-LUSO | 38.0 | 26.4 | 17.9 | 0.7 | 0.1 | 0.1 | 4658 |
| | β-HOSO | 0.3 | 0.2 | 10.0 | 0.4 | 24.7 | 42.8 | (0.0088) |
| [**8**˙]$^+$ | β-LUSO | 28.8 | 25.9 | 23.5 | 3.8 | 2.3 | 1.4 | 4812 |
| | β-HOSO | 3.8 | 2.3 | 10.5 | 0.4 | 24.6 | 35.6 | (0.09023) |
| [**8a**˙]$^+$ | β-LUSO | 29.0 | 24.6 | 23.7 | 3.9 | 2.7 | 2.1 | 4378 |
| | β-HOSO | 5.4 | 3.2 | 12.1 | 0.5 | 23.2 | 36.2 | (0.1024) |

[a] LH20t/def2-SVP// LH20t-D3(BJ)/def2-SVP, COSMO ($CH_2Cl_2$).

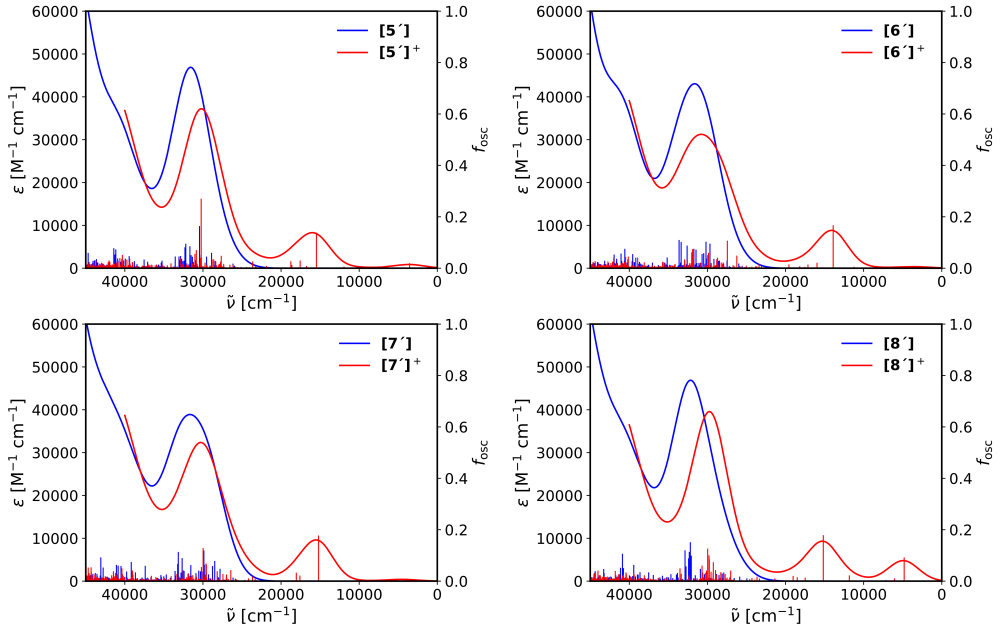


**Figure S1**. UV-Vis-NIR spectra for **[5´]** – **[8´]** and **[5´]**$^{+}$ – **[8´]**$^{+}$ from TDDFT calculations at the LH20t/def2-SVP//LH20t-D3(BJ)/def2-SVP, COSMO ($CH_2Cl_2$) level of theory. For each spectrum, 400 vertical excitation energies were calculated (stick spectra, $f_{osc}$ axis) and broadened with Gaussian line shapes with linewidths of 1900 cm$^{-1}$ (line spectra, $\varepsilon$ axis).

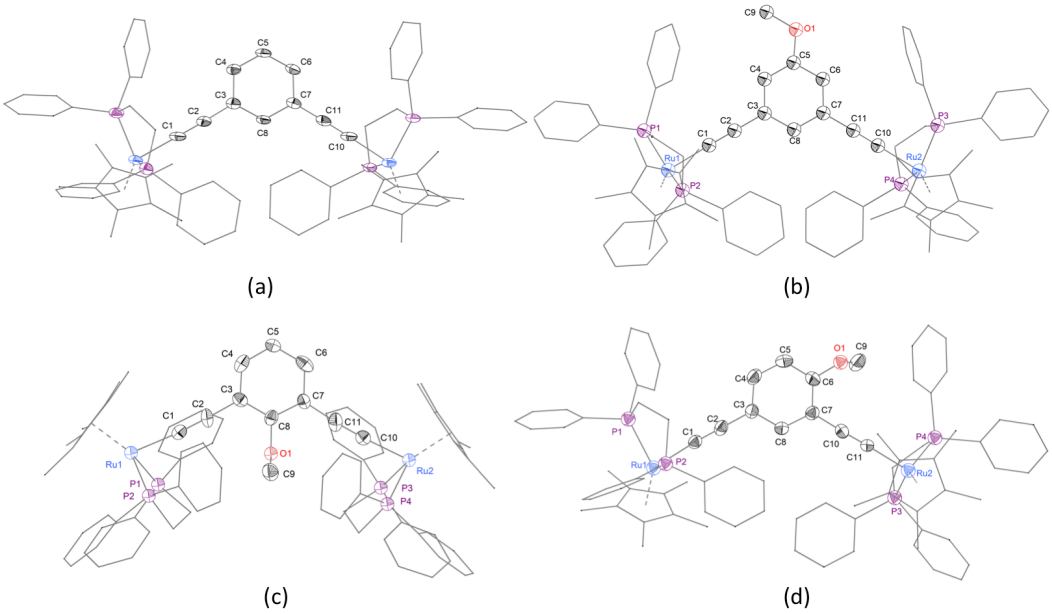


**Figure S2.** Plots of the molecular structures of (a) **5**, (b) **6**, (c) **7**, and (d) **8** showing the crystallographic atom labelling scheme. Thermal ellipsoids plotted at 50 % probability level.

**Table S3.** Crystallographic and refinement details

| | **5** | **6** | **7** | **8** |
|---|---|---|---|---|
| CCDC Number | 2163741 | 2163064 | 2163065 | 2163066 |
| Empirical formula | $C_{82}H_{74}P_4Ru_2$ | $C_{83}H_{84}OP_4Ru_2$ | $C_{83}H_{84}OP_4Ru_2$ | $C_{83}H_{84}OP_4Ru_2{\cdot}0.67CH_2Cl_2$ |
| Formula weight | 1385.43 | 1423.52 | 1423.52 | 1479.99 |
| Temperature/K | 101(2) | 100.0(10) | 150.00(10) | 119.95(10) |
| Crystal system | *monoclinic* | *monoclinic* | *monoclinic* | *triclinic* |
| Space group | $P2_1/c$ | $P2_1/c$ | $P2_1/c$ | $P\bar{1}$ |
| *a*/Å | 19.2514(3) | 19.2623(4) | 18.8881(3) | 14.4062(3) |
| *b*/Å | 21.9024(3) | 17.0102(3) | 20.8050(3) | 16.3949(5) |
| *c*/Å | 33.7227(6) | 21.9453(4) | 19.5529(3) | 17.3566(5) |
| *α*/° | 90 | 90 | 90 | 114.700(3) |
| *β*/° | 103.878(2) | 103.9989(19) | 103.523(2) | 95.821(2) |
| *γ*/° | 90 | 90 | 90 | 99.324(3) |
| *V*/Å$^3$ | 13804.2(4) | 6977.0(2) | 7470.6(2) | 3609.16(19) |
| *Z* | 8 | 4 | 4 | 2 |
| $\rho_{calc}$ g/cm$^3$ | 1.333 | 1.355 | 1.266 | 1.362 |
| *μ*/mm$^{-1}$ | 4.749 | 0.571 | 4.409 | 5.03 |
| *F*(000) | 5712 | 2952 | 2952 | 2704 |
| Crystal size/mm$^3$ | 0.203×0.165×0.029 | 0.4×0.2×0.2 | 0.200×0.150×0.100 | |
| Radiation | CuKα ($\lambda$ = 1.54184 Å) | MoKα ($\lambda$ = 0.71073 Å) | CuKα ($\lambda$ = 1.54184 Å) | CuKα ($\lambda$ = 1.54184 Å) |
| *Θ* range for data collection/° | 3.108 to 66.493 | 3.270 to 25.998 | 2.406 to 66.493 | 3.8200 to 65.9880 |
| Index ranges | $-21 \le h \le 22$, $-25 \le k \le 16$, $-40 \le l \le 39$ | $-23 \le h \le 22$, $-20 \le k \le 20$, $-24 \le l \le 27$ | $-22 \le h \le 22$, $-24 \le k \le 24$, $-23 \le l \le 22$ | $-17 \le h \le 15$, $-19 \le k \le 19$, $-20 \le l \le 20$ |
| Reflections collected | 86555 | 37564 | 103381 | 50804 |
| Independent reflections | 23980 ($R_{int}$ = 0.0643) | 13664 ($R_{int}$ = 0.0320) | 13141 [$R_{int}$ = 0.1188] | 12825 [$R_{int}$ = 0.0658] |
| Data/restraints /parameters | 23980/1560/1566 | 13664/1052/883 | 13141/839/853 | 12825/4/839 |
| Goodness-of-fit on $F^2$ | 1.086 | 1.079 | 1.106 | 1.025 |
| Final *R* indexes [$I \ge 2\sigma(I)$] | $R_1$ = 0.1406, $wR_2$ = 0.3573 | $R_1$ = 0.0327, $wR_2$ = 0.0689 | $R_1$ = 0.1063, $wR_2$ = 0.3338 | $R_1$ = 0.0542, $wR_2$ = 0.1316 |
| Final *R* indexes [all data] | $R_1$ = 0.1542, $wR_2$ = 0.3654 | $R_1$ = 0.0465, $wR_2$ = 0.0722 | $R_1$ = 0.1196, $wR_2$ = 0.3407 | $R_1$ = 0.0763, $wR_2$ = 0.1498 |
| Largest diff. peak/hole / e Å$^{-3}$ | 10.304/–1.866 | 0.520/–0.445 | 2.702/–1.479 | 2.801/–2.217 |

**Table S4.** Selected crystallographically determined bond lengths (Å) and angles (°).

| | **5** | **6** | **7** | **8** |
|---|---|---|---|---|
| Ru1–P1 | 2.253(3)<br>2.266(3) | 2.2755(6) | 2.264(3) | 2.2471(12) |
| Ru1–P2 | 2.262(3)<br>2.260(3) | 2.2541(6) | 2.264(3) | 2.2662(12) |
| Ru1–C1 | 1.986(6) | 2.001(2) | 1.968(12) | 2.014(5) |
| C1≡C2 | 1.243(8)<br>1.242(8) | 1.213(3) | 1.230(17) | 1.214(7) |
| C2–C3 | 1.421(7)<br>1.421(7) | 1.436(3) | 1.447(17) | 1.429(7) |
| C7–C11 | 1.418(12)<br>1.424(12) | 1.437(3) | 1.423(17) | 1.434(7) |
| C10≡C11 | 1.242(8)<br>1.243(8) | 1.211(3) | 1.229(17) | 1.204(8) |
| C10–Ru2 | 1.986(6) | 1.997(2) | 2.016(12) | 2.011(5) |
| Ru2–P3 | 2.258(3)<br>2.236(3) | 2.2631(6) | 2.252(3) | 2.2486(13) |
| Ru2–P4 | 2.263(3)<br>2.248(3) | 2.2483(6) | 2.264(3) | 2.2590(14) |
| P1–Ru1–P2 | 82.66(12)<br>83.59(11) | 83.91(2) | 83.60(11) | 83.76(5) |
| Ru1–C1≡C2 | 179.4(11)<br>175.4(11) | 176.33(19) | 177.0(11) | 176.0(5) |
| C1≡C2–C3 | 178.0(12)<br>175.8(12) | 175.0(2) | 174.7(13) | 173.2(6) |
| P3–Ru2–P4 | 83.32(11)<br>83.39(11) | 84.50(2) | 84.11(10) | 82.68(5) |
| Ru2–C10≡C11 | 177.9(10)<br>178.7(11) | 175.12(19) | 175.1(10) | 176.1(5) |
| C10≡C11–C7 | 173.0(12)<br>177.4(12) | 176.5(2) | 177.2(12) | 177.8(6) |

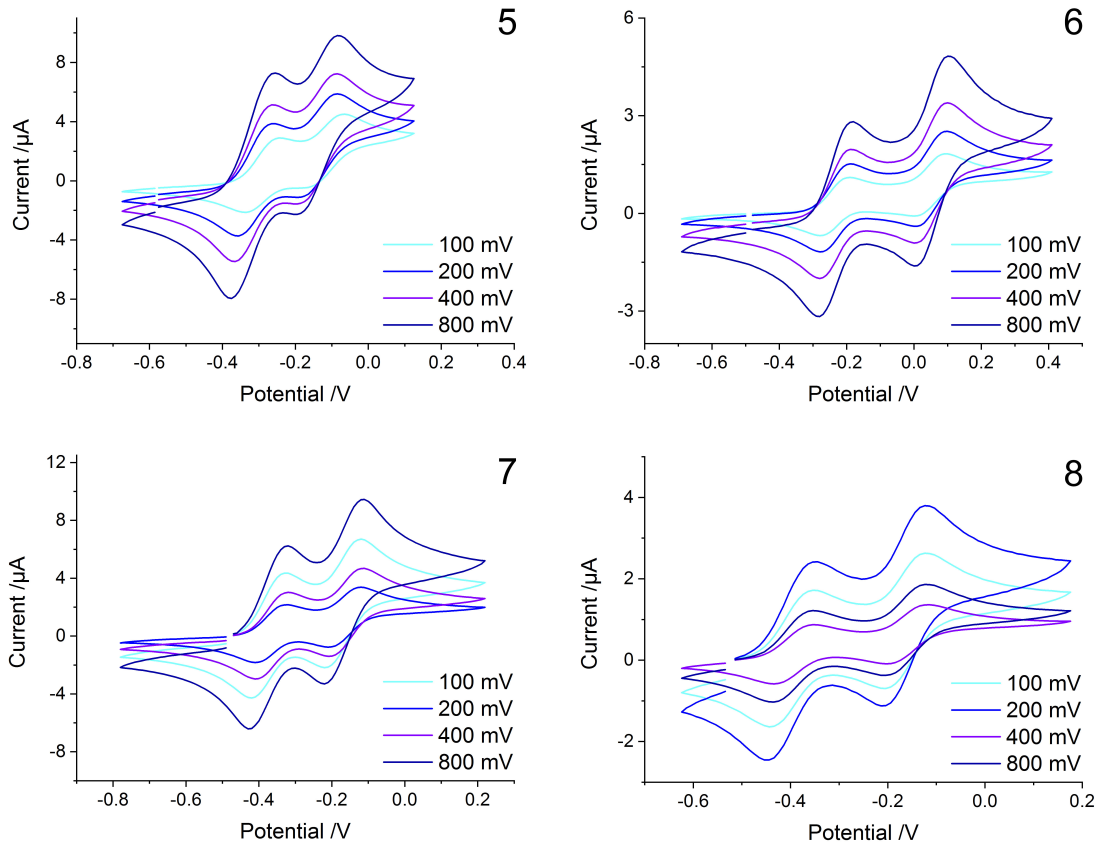


**Figure S3.** Plots of the cyclic voltammograms (CV) data for complexes **5** – **8** ($CH_2Cl_2$, 0.1 M $NBu_4PF_6$, room temperature) vs ferrocene/ferricenium [$E_{1/2}(Fc/Fc^+)$ = 0 V] at a platinum working electrode.

**Table S4.** Summary of electrochemical response of complexes **5** – **8**.[a]

| | $E^1_{1/2}$ (V) | $E^2_{1/2}$ (V) | $\Delta E^{1\text{-}2}$ (V) |
|---|---|---|---|
| **5**[1] | –0.30 | –0.09 | 0.21 |
| **6** | –0.37 | –0.16 | 0.21 |
| **7** | –0.40 | –0.17 | 0.23 |
| **8** | –0.23 | 0.06 | 0.29 |

[a] Data collected by cyclic voltammetry in $CH_2Cl_2$ solution containing 0.1 M $NBu_4PF_6$ supporting electrolyte, using Pt disc working, Pt wire pseudo-reference and counter electrodes. Potentials are reported against the ferrocene / ferrocenium couple ($E(Fc/Fc^+)$ = 0.00 V).[2]

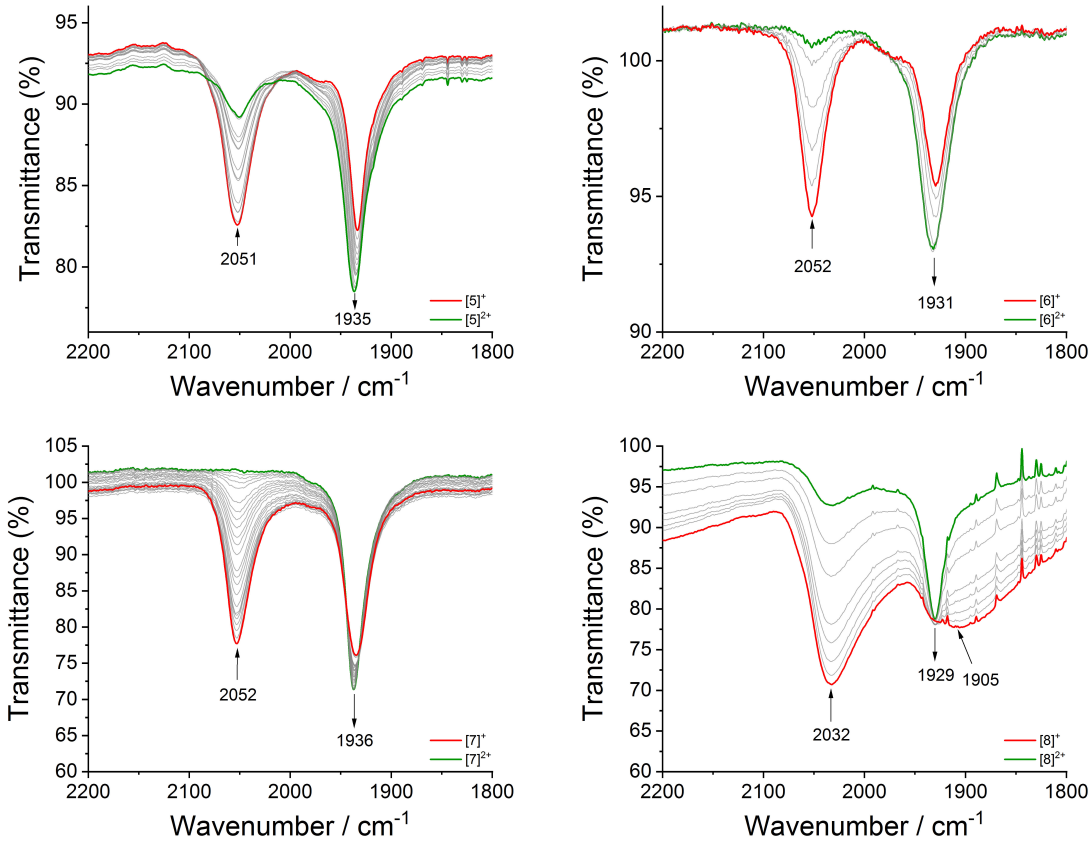


**Figure S4.** IR spectra collected during the oxidation of [**5** – **8**]$^{+}$ to [**5** – **8**]$^{2+}$ in a spectroelectrochemical cell ($CH_2Cl_2$ / 0.1 M $NBu_4PF_6$).

**Table S5.** Computational results for the harmonic vibrational frequencies (in $cm^{-1}$) of the ν(C≡C) bands.[a]

| | [**5**´] | [**5**´]$^{+}$ | [**6**´] | [**6**´]$^{+}$ | [**7**´] | [**7**´]$^{+}$ | [**8**´] | [**8**´]$^{+}$ |
|---|---|---|---|---|---|---|---|---|
| | *raw results* | | | | | | | |
| $\nu_1$(C≡C) | 2172 | 2044 | 2185 | 2049 | 2178 | 2047 | 2187 | 2065 |
| $\nu_2$(C≡C) | 2179 | 2170 | 2196 | 2180 | 2188 | 2158 | 2193 | 2153 |
| | *scaled with an empirical scaling factor of 0.9391* | | | | | | | |
| $\nu_1$(C≡C) | 2040 | 1920 | 2052 | 1924 | 2045 | 1923 | 2053 | 1939 |
| $\nu_2$(C≡C) | 2046 | 2038 | 2063 | 2047 | 2055 | 2027 | 2060 | 2022 |

[a] LH20t-D3(BJ)/def2-SVP, COSMO($CH_2Cl_2$).

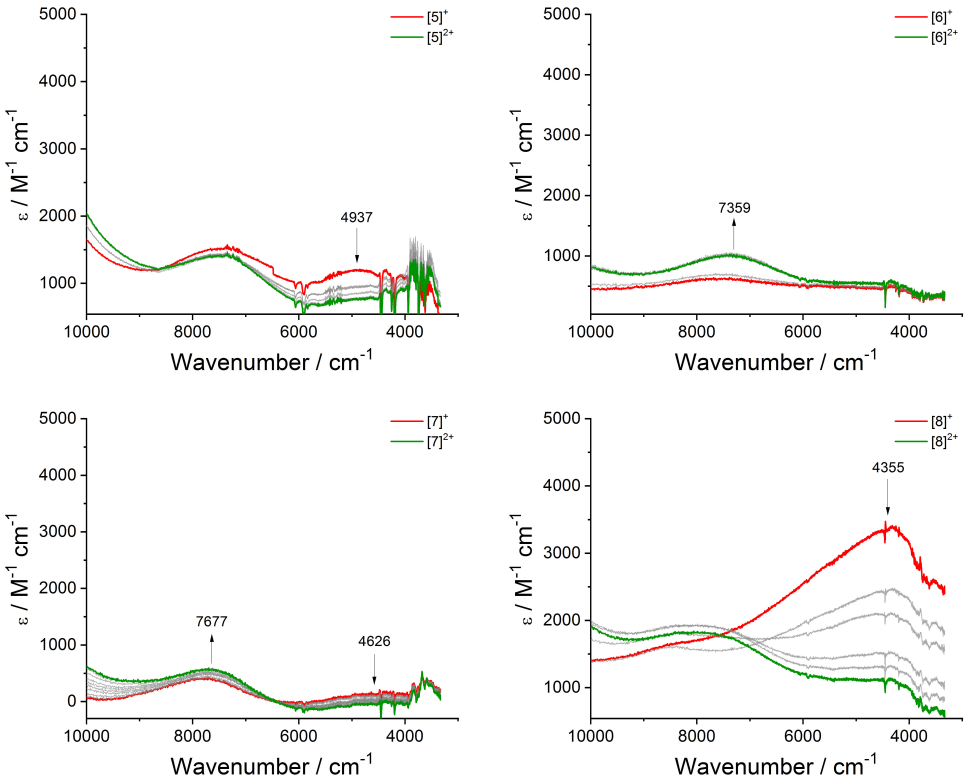


**Figure S5.** NIR spectra collected during the oxidation of [**5** – **8**]$^{+}$ to [**5** – **8**]$^{2+}$ in a spectroelectrochemical cell ($CH_2Cl_2$ / 0.1 M $NBu_4PF_6$) illustrating the collapse of the low-energy IVCT transition.

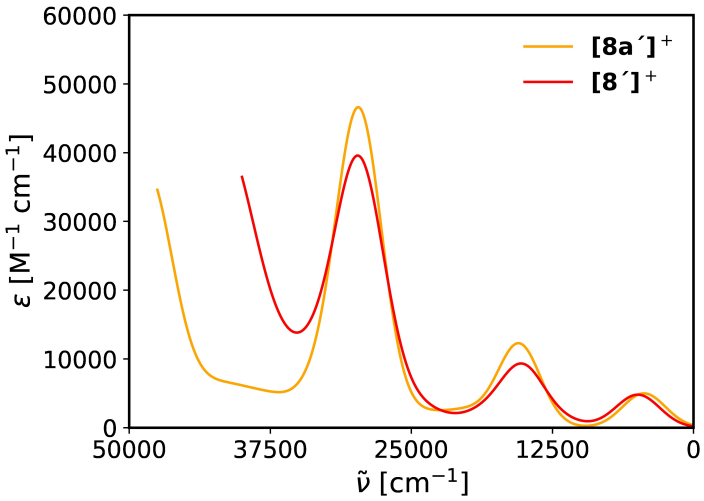


**Figure S6.** Comparison of the UV-Vis-NIR spectra of [**8a´**]$^{+}$ and [**8´**]$^{+}$ obtained from TDDFT calculations at the LH20t/def2-SVP//LH20t-D3(BJ)/def2-SVP, COSMO ($CH_2Cl2$) level of theory broadened with Gaussian line shapes with linewidths of 1900 cm$^{-1}$.

## Experimental

*General conditions:* All reactions reported below were performed under an atmosphere of nitrogen employing standard Schlenk techniques. Unless otherwise stated, no specific care was taken to exclude air during workup of reactions. Solvents were dried by literature methods or using an Innovative Technologies Solvent Purification System and sparged with nitrogen before use. Silica gel was used as acquired with no pre-treatment prior to chromatography.

*Instrumentation*: $^{1}$H, $^{13}$C{$^{1}$H} and $^{31}$P{$^{1}$H} spectra were recorded on Varian 400 MHz ($^{1}$H: 399.86 MHz, $^{13}$C: 100.6 MHz, $^{31}$P: 161.9 MHz) and Bruker 500 MHz ($^{1}$H: 500.10 MHz, $^{13}$C: 125.8 MHz, $^{31}$P: 202.4 MHz) spectrometers at room temperature. Chemical shifts are all reported relative to residual solvent peaks. All $^{31}$P NMR were referenced to a $H_3PO_4$ (85 %) external standard. IR spectra were recorded on either Agilent Cary 630 or Cary 670 FTIR spectrometers using ATR or transmission methods, the later in a solution cell fitted with $CaF_2$ windows. Mass spectra were obtained from a Waters Liquid Chromatograph Premier Mass Spectrometer, using positive mode Atmospheric Pressure Chemical Ionisation (APCI(+)) or Electrospray Ionisation (ESI(+)). Samples were prepared in MeCN and inserted by direct injection. Electrochemical studies were carried out using an Emstat$^{3+}$ potentiostat, with platinum working, counter and pseudo-reference electrodes, from solutions in $CH_2Cl_2$ containing 0.1 M $NBu_4PF_6$ as supporting electrolyte, $\nu$ = 100 – 800 $mVs^{-1}$. The ferrocene/ferrocinium ($E$(Fc/Fc$^{+}$) = 0.00 V) or decamethylferrocene/decamethylferrocenium ($E$(DMFc/DMFc$^{+}$) = −0.55 V)[1b] couple were employed as an internal references for potential measurements.[2]

Spectroelectrochemical studies were conducted in a transmission cell of Hartl design fitted with $CaF_2$ widows,[3] and controlled by the EmStat$^{3+}$ from solutions of the analyte (ca.1 mM) in 0.1 M $NBu_4PF_6/CH_2Cl_2$. Data were recorded on Cary5000 UV-vis-NIR and Cary 660 FT-IR/NIR spectrometers. The spectroelectrochemical data were collected in two individual cells, each with Ag wire pseudo-reference electrodes, which differ vs the voltammetry data collected in a conventional voltammetry cell (reference vs Fc) given in Table S4. As these spectroelectrochemical cells are hand-crafted, the position of the working, counter and reference electrodes are unavoidably different when placed between the windows of the <150μm pathlength cell. This results in different degree of uncompensated solution resistance cell to cell. The different thickness of the thin layer cell to cell also results in different diffusion characteristics at the edges of the semi-transparent Pt-gauze working electrodes and residual currents flowing through the cell even when equilibrium has been reached in the small solution volume within beampath. We therefore use the spectroscopic data, including observation of tight isosbestic, to determine when electrolysis in the beam path is complete, rather than absolute applied potentials, which are as follows

**5 SEC** $E^1_{1/2}$ +0.25 V, $E^2_{1/2}$ +0.29 V; **CV** $E^1_{1/2}$ -0.30 V, $E^2_{1/2}$ -0.09 V

**6 SEC** $E^1_{1/2}$ +0.26 V, $E^2_{1/2}$ +0.40 V; **CV** $E^1_{1/2}$ -0.37 V, $E^2_{1/2}$ -0.16 V

**7 SEC** $E^1_{1/2}$ +0.17 V, $E^2_{1/2}$ +0.23 V; **CV** $E^1_{1/2}$ -0.40 V, $E^2_{1/2}$ -0.17 V

**8 SEC** $E^1_{1/2}$ +0.20 V, $E^2_{1/2}$ +0.40 V; **CV** $E^1_{1/2}$ -0.23 V, $E^2_{1/2}$ +0.06 V

The compounds 3,5-bis(trimethylsilylethynyl)anisole,[4] 2,6-bis(trimethylsilylethynyl)anisole,[4b, 5] 2,4-bis(trimethylsilylethynyl)anisole,[4b] RuCl(dppe)Cp*[6] and **5**[1a] were prepared by literature methods, or minor variations as described below. All other compounds were purchased and used as received.

*Syntheses*

**General Procedure for the Synthesis of Ruthenium Bis(acetylide) Complexes 5 – 8**

A suspension of RuCl(dppe)Cp* (2 equiv.), the bis(trimethylsilylethynyl) anisole (1 equiv.) and KF (3 equiv.) in MeOH (15 mL) was stirred and heated at reflux point (65 °C) overnight (16 h) during which time a yellow precipitate formed. The reaction mixture was cooled to 0 °C before solids were collected by filtration, washed with MeOH (2 x 5 mL) and hexanes (2 x 5 mL) to give the desired products. Recrystallisation afforded single crystals suitable for X-ray diffraction.

**Synthesis of [{Cp*(dppe)Ru(C≡C)}$_2$(μ-1,3-C$_6$H$_4$)] (5)**

From RuCl(dppe)Cp* (0.100 g, 0.15 mmol), 1,3-bis(trimethylsilylethynyl)benzene (0.05 g, 0.19 mmol) and KF (0.011 g, 0.23 mmol) as described above, **5** was obtained as a yellow precipitate (0.14 g, 0.11 mmol, 70 %). Crystals suitable for single-crystal X-ray diffraction were grown by slow diffusion of $Et_2O$ into a $CH_2Cl_2$ solution of the complex containing 5% $NEt_3$. IR ($CH_2Cl_2$ / cm$^{-1}$): 2060 ν(C≡C); 1423 ν(Ar). $^1$H NMR ($CDCl_3$, 500 MHz) $\delta$ /ppm 7.80 (m, 8H, H$^o$); 7.27 (m, 24H, H$^{p/m}$); 7.20 (m, 8H, H$^o$); 6.70 (t, 1H, H$^5$); 6.70 (t, 1H, H$^6$); 6.40 (dd, 2H, H$^4$); 2.73 (m, 4H, dppe); 2.09 (m, 4H, dppe); 1.62 (s, 30H, Cp*). $^{13}$C{$^1$H} NMR ($CDCl_3$, 125.8 MHz) $\delta$ /ppm: 139.2 (m, C$^5$); 139.0 (m, C$^i$); 137.1 (m, C$^i$); 133.9 (m, C$^o$); 133.4 (m, C$^o$); 132.0 (s, C$^6$); 130.5 (s, C$^3$); 128.9 (d, C$^p$); 127.5 (m, C$^m$); 127.3 (m, C$^m$); 126.8 (s, C$^5$); 125.6 (s, C$^4$); 125.1 (s, C$^1$); 110.0 (s, C$^2$); 92.6 (s, Cp$^*$); 29.7 (m, dppe); 10.2 (s, Me at Cp*). $^{31}$P{$^1$H} NMR ($CDCl_3$ 161.9 MHz) $\delta$ /ppm: 80.9. APCI-MS (*m*/*z*): Calculated for [M+H]$^+$ [$C_{82}H_{83}P_4Ru_2$]$^+$ 1395.3532 amu; observed 1395.3598 amu.

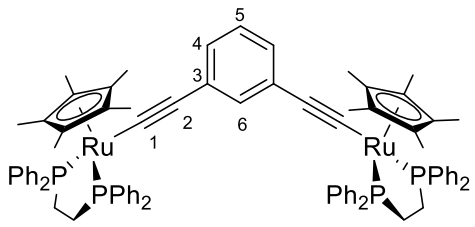

**Synthesis of [{Cp*(dppe)Ru(C≡C)}$_2$(μ-1,3-C$_6$H$_3$-5-OMe)] (6)**

From RuCl(dppe)Cp* (0.21 g, 0.31 mmol), 3,5-bis(trimethylsilylethynyl)anisole (0.045 g, 0.15 mmol) and KF (0.010 g, 0.18 mmol) as described above, **6** was obtained as a yellow precipitate (0.15 g, 0.11 mmol, 70 %). Crystals suitable for X-ray diffraction were obtained by slow diffusion ($CH_2Cl_2$ / hexanes). IR ($CH_2Cl_2$, $cm^{-1}$): 2061 ν(C≡C); 1423 ν(Ar). $^1$H NMR ($CDCl_3$, 500 MHz) $\delta$ /ppm 7.80 (m, 8H, H$^o$), 7.28 (m, 24H, H$^{p/m}$), 7.21 (m, 8H, H$^o$), 6.37 (s, 1H, H$^6$), 5.96 (s, 2H, H$^4$), 3.56 (s, 3H, H$^7$), 2.73 (m, 4H, dppe), 2.09 (m, 4H, dppe), 1.58 (Cp*). $^{13}$C{$^1$H} NMR ($CDCl_3$, 125.8 MHz) $\delta$ /ppm 158.6 (s, C$^5$), 139.2 (m, C$^i$), 137.3 (m, C$^i$), 134.0 (m, C$^o$), 133.5 (m, C$^o$), 131.4 (s, C$^2$), 129.0 (s, C$^p$), 127.5 (m, C$^m$), 127.4 (m, C$^m$), 125.7 (m, C$^1$), 125.5 (s, C$^6$), 111.5 (s, C$^4$), 110.0 (s, C$^2$), 92.7 (s, Cp$^*$), 55.2 (s, C$^7$), 29.7 (m, dppe), 10.3 (s, Me at Cp*). $^{31}$P{$^1$H} NMR ($CDCl_3$ 161.9 MHz) $\delta$ /ppm: 81.6. APCI-MS (*m*/*z*): Calculated for $[M+H]^+$ $[C_{83}H_{85}OP_4Ru_2]^+$ 1425.3638 amu; observed 1425.3630 amu.

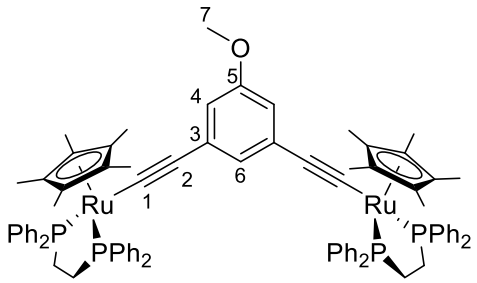

**Synthesis of [{Cp*(dppe)Ru(C≡C)}$_2$(μ-1,3-C$_6$H$_3$-2-OMe)] (7)**

From RuCl(dppe)Cp* (0.25 g, 0.37 mmol), 2,6-bis(trimethylsilylethynyl)anisole (0.053 g, 0.17 mmol) and KF (0.010 g, 0.17 mmol) as described above, **7** was obtained as a yellow precipitate (0.170 g, 0.12 mmol, 71 %). Crystals suitable for X-ray diffraction were grown by slow diffusion ($CH_2Cl_2$ / pentane). IR ($CH_2Cl_2$, $cm^{-1}$): 2062 ν(C≡C); 1422 ν(Ar). $^1$H NMR ($CDCl_3$, 500 MHz) $\delta$ /ppm: 7.80 (m, 8H, H$^o$); 7.31 (m, 4H, H$^p$); 7.26 (m, 20H, H$^{p/m}$); 7.17 (m, 8H, H$^o$); 6.46 (m, $J_{6,5}$ = 6.8 Hz, $J_{6,5'}$ = 6.8 Hz, 1H, H$^6$); 6.40 (d, $J_{5,6}$ = 6.8 Hz, 2H, H$^5$); 2.97 (s, 3H, H$^7$); 2.87 (m, 4H, dppe); 2.13 (m, 4H, dppe); 1.58 (s, 30H, Cp*).$^{13}$C{$^1$H} NMR ($CDCl_3$, 125.8 MHz) $\delta$ /ppm: 159.9 (s, C$^4$); 139.3 (m, C$^i$); 137.5 (m, C$^i$); 134.0 (m, C$^o$); 133.5 (m, C$^o$); 128.8 (s, C$^p$), 128.8 (s, C$^p$); 128.5 (m, C$^1$); 127.8 (s, C$^5$); 127.5 (m, C$^m$); 127.4 (m, C$^m$); 124.3 (s, C$^3$); 122.0 (s, C$^6$); 106.5 (s, C$^2$); 92.8 (s, Cp$^*$); 59.2 (s, C$^7$); 29.6 (m, dppe); 10.3 (s, Me at Cp$^*$). $^{31}$P{$^1$H} NMR ($CDCl_3$ 161.9 MHz) $\delta$ /ppm: 81.8. APCI (*m/z*): Calculated for [M+H]$^+$ [$C_{83}H_{85}OP_4Ru_2$]$^+$ 1425.3638 amu; observed 1425.3645 amu.

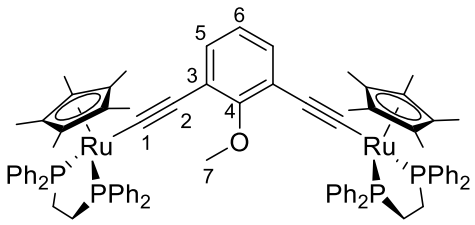

**Synthesis of [{Cp*(dppe)Ru(C≡C)}$_2$(μ-1,3-C$_6$H$_3$-4-OMe)] (8)**

From RuCl(dppe)Cp* (0.20 g, 0.30 mmol), 2,4-bis(trimethylsilylethynyl)anisole (0.044 g, 0.15 mmol) and KF (0.011 g, 0.19 mmol) as described above, **8** was obtained as a yellow precipitate (0.14 g, 0.098 mmol, 66 %). Crystals for single-crystal X-ray diffraction were obtained by slow diffusion ($CH_2Cl_2$ / pentane). IR ($CH_2Cl_2$, $cm^{-1}$): 2065 ν(C≡C); 1484 ν(Ar). $^1$H NMR ($CDCl_3$, 500 MHz) $\delta$ /ppm: 7.83 (m, 4H, H$^o$); 7.82 (m, 4H, H$^o$); 7.29 (m, 12H, H$^{p/m}$); 7.22 (m, 16H, H$^{o/p/m}$); 7.14 (m, 4H, H$^o$); 6.76 (s, 1H, H$^4$); 6.44 (d, $J_{9,10}$ = 8.5 Hz, 1H, H$^9$); 6.38 (d, $J_{10,9}$ = 8.5 Hz, 1H, H$^{10}$); 3.44 (s, 3H, H$^{11}$); 2.93 (m, 2H, dppe); 2.73 (m, 2H, dppe); 2.18 (m, 2H, dppe); 2.09 (m, 2H, dppe); 1.60 (s, 15H, Cp*); 1.58 (s, 15H, Cp*). $^{13}$C{$^1$H} NMR ($CDCl_3$, 125.8 MHz) $\delta$ /ppm: 156.6 (s, C$^8$); 139.3 (m, C$^i$); 137.6 (m, C$^i$); 134.3 (s, C$^4$); 134.0 (m, C$^o$); 133.5 (m, C$^o$); 129.3 (m, C$^1$); 128.9 (s, C$^p$); 128.8 (s, C$^p$); 127.5 (m, C$^m$); 127.3 (m, C$^m$); 125.7 (s, C$^{10}$); 124.1 (s, C$^3$); 121.0 (m, C$^7$); 120.6 (s, C$^5$); 111.6 (s, C$^9$); 109.0 (s, C$^2$); 105.7 (s, C$^6$); 92.8 (m, Cp$^*$); 92.6 (m, Cp$^*$); 56.3 (s, C$^{11}$); 29.7 (m, dppe); 10.3 (s, Me at Cp$^*$); 10.3 (s, Me at Cp$^*$). $^{31}$P{$^1$H} NMR ($CDCl_3$ 161.9 MHz) $\delta$ /ppm: 81.9; 81.7. APCI (*m/z*): Calculated for [M+H]$^+$ [$C_{83}H_{85}OP_4Ru_2$]$^+$ 1425.3638 amu; observed 1425.3634 amu.

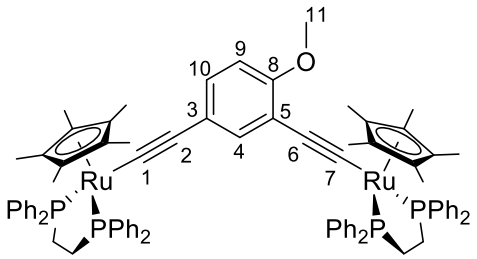

*Crystallography*

Data for **5**–**8** were collected using an Oxford Diffraction Gemini diffractometer with graphite-monochromated Mo Kα (λ = 0.71073 Å) (**6**) and Cu Kα radiation (λ = 1.54184 Å) (**8**), or an XtaLAB Synergy Single source HyPix diffractometer with Cu Kα radiation (λ = 1.54184 Å) using a PhotonJet X-ray Source (**5**, **7**), at 100 (**5**,**6**), 150 (**7**) and 120 K (**8**). The data were corrected for Lorentz and polarization effects and absorption. The structures were solved with the ShelXT 2018 solution program using dual methods,[7] implemented in the graphical interfaces of Olex2 1.5[8] or WinGX 2018.3,[9] and refined with ShelxXL[10] using full matrix least squares minimization on $F^2$. The diffraction pattern was indexed and the total number of runs and images was based on the strategy calculation from the program CrysAlisPro.[11] Data reduction, scaling and absorption corrections were performed using CrysAlisPro. Anisotropic displacement parameters were employed for the non-hydrogen atoms. All hydrogen atoms were added at calculated positions and refined by use of a riding model with isotropic displacement parameters based on those of the parent atom. Crystallographic data for the structures reported in this paper are reported in Table S3 and have been deposited at the Cambridge Crystallographic Data Centre (2163741, 2163064 – 2163066). Copies of the data can be obtained free of charge via https://www.ccdc.cam.ac.uk/structures/, or from the Cambridge Crystallographic Data Centre, 12 Union Road, Cambridge CB2 1EZ, U.KCB21EZ, UK (fax +441223336033; email deposit@ccdc.cam.ac.uk).

*Quantum chemical calculations*

All quantum chemical calculations were performed with a developers' version of TURBOMOLE equivalent to release V7.6.[12] [13] The local hybrid (LH) functional

LH20t[14] was used in all (TD)DFT calculations. LH20t was developed with a good balance between (de)localization and left-right correlation in mind and does indeed perform excellent for both dedicated benchmark sets such as the MVO10 test set[14-15] and real-world MV transition metal complexes.[14] [16] In contrast to previous investigations on similar MV systems[17] [16] that used the global hybrid functional BLYP35[18] for the structure optimizations, here, LH20t is used throughout to fully benefit from these advantages, which indeed results in lower spin contamination of the ground states and slightly more delocalized spin densities compared to initial test calculations with the BLYP35 functional (Table S6). Moreover, initial test calculations at the BLYP35/6-31G** level found the β-HOSO → β-LUSO IVCT band to be too high in energy at 7950 $cm^{-1}$ for **[8′]**$^{+}$ whereas the LH20t/def2-SVP calculation is in much better agreement with the experiment (4812 $cm^{-1}$, Table S2, Figure 3). Notably, also the demanding numerical calculations of vibrational frequencies via TURBOMOLE's NumForce script (central differences, 0.01 bohr displacements) were done with LH20t thus demonstrating the efficiency of the LH implementation also in large-scale applications. Vibrational frequencies were corrected for systematic errors, e.g., due to the harmonic approximation, via an empirical scaling factor[19] of 0.9391, which was deduced from a comparison of the experimental C≡C stretching mode for the ethyne molecule (NIST Webbook: 1974 $cm^{-1}$)[20] and a gas phase calculation at the computational level described in this section (2102 $cm^{-1}$). def2-SVP basis sets[21] with the associated quasirelativistic effective core potential for Ru (def2-ECP)[22] were used throughout, together with the corresponding auxiliary basis sets for the resolution of the identity approximation

applied for the Coulomb part.[23] A medium sized numerical integration grid (TURBOMOLE gridsize 3) was used and grid weight derivatives were included in the calculation of gradients during the optimization and frequency calculations. Ground state calculations were converged to at least $10^{-8}$ $E_h$. In TDDFT calculations, up to 400 vertical excitation vectors and energies were calculated. Dispersion interactions have been accounted for by using the DFT-D3[24] approach with a Becke-Johnson (BJ)[25] damping function ($s_6$ = 1.0, $s_8$ = 6.878507, $a_1$ = 0.547562, $a_2$ = 6.648749). All calculations used the conductor-like screening model (COSMO)[26] to account for solvent effects at the level of a continuum model (DCM solvent: $\varepsilon$ = 8.93, $n$ = 1.424).

To assess the basis set incompleteness error of the def2-SVP basis set in the TDDFT calculations of the systems under investigation, calculations with def2-TZVP,[21] def2-TZVPP,[21] and def2-QZVPP[21] basis sets were carried out for [**5a'**]$^+$ (Table S7). With the def2-QZVPP basis set, basis set convergence is essentially reached as indicated by matching oscillator strengths in the length and velocity representation. On average, excitation energies with the def2-SVP basis set deviate by 0.04 eV (320 cm$^{-1}$) from the def2-QZVPP results showing sufficient convergence already at this moderate sized double-ζ basis set size.

**Table S6.** Spin contamination ($\zeta = < S^2 >_{\mathrm{exact}} - < S^2 >_{\mathrm{DFT}}$) and atomic populations with the LH20t protocol and BLYP35-based calculations for comparison for two selected systems.[a]

| | BLYP35/ def2-SVP// BLYP35/LANL2DZ(Ru), 6-31G**[a] | | | LH20t/def2-SVP// BLYP35/LANL2DZ(Ru), 6-31G**[a] | | | LH20t/def2-SVP// LH20t-D3-BJ/def2-SVP[a] | | |
|---|---|---|---|---|---|---|---|---|---|
| | | atomic populations from spin density[b] | | | atomic populations from spin density[b] | | | atomic populations from spin density[b] | |
| | $\zeta$ | Ru(1) | Ru(2) | $\zeta$ | Ru(1) | Ru(2) | $\zeta$ | Ru(1) | Ru(2) |
| **[5']$^+$** | 0.0311 | 0.695 | -0.001 | 0.0155 | 0.598 | 0.000 | 0.0150 | 0.474 | 0.001 |
| **[8']$^+$** | 0.0349 | 0.575 | -0.001 | 0.0154 | 0.480 | 0.012 | 0.0142 | 0.395 | 0.017 |

[a]All calculations with COSMO ($CH_2Cl_2$).
[b]Atomic populations are from NPA calculations.

**Table S7.** Basis set convergence for TDDFT calculations (LH20t, COSMO($CH_2Cl_2$)) for the first five excitations of [**5a**$^-$]$^+$ and deviations from calculations with the def2-QZVPP basis set.[a]

| **def2-SVP** | | | | |
|---|---|---|---|---|
| #Excitation | $\Delta E$ [eV] | $f_{\mathrm{osc}}^{\mathrm{vel}}$ | $f_{\mathrm{osc}}^{\mathrm{len}}$ | $\Delta E - \Delta E^{\text{def2-QZVPP}}$ [eV] |
| 1 | 0.5348 | 0.0177 | 0.0192 | -0.0645 |
| 2 | 0.7197 | 0.0000 | 0.0003 | 0.0311 |
| 3 | 1.1254 | 0.0010 | 0.0012 | -0.0164 |
| 4 | 1.1499 | 0.0001 | 0.0007 | -0.0415 |
| 5 | 1.5123 | 0.0007 | 0.0007 | -0.0434 |
| MAD | | | | 0.0394 |
| MaxSD | | | | -0.0645 |
| **def2-TZVP** | | | | |
| # Excitation | $\Delta E$ [eV] | $f_{\mathrm{osc}}^{\mathrm{vel}}$ | $f_{\mathrm{osc}}^{\mathrm{len}}$ | $\Delta E - \Delta E^{\text{def2-QZVPP}}$ [eV] |
| 1 | 0.5854 | 0.0201 | 0.0213 | -0.0139 |
| 2 | 0.7035 | 0.0001 | 0.0003 | 0.0149 |
| 3 | 1.1479 | 0.0013 | 0.0016 | 0.0060 |
| 4 | 1.1887 | 0.0003 | 0.0004 | -0.0028 |
| 5 | 1.5563 | 0.0007 | 0.0007 | 0.0006 |
| MAD | | | | 0.0076 |
| MaxSD | | | | 0.0149 |
| **def2-TZVPP** | | | | |
| # Excitation | $\Delta E$ [eV] | $f_{\mathrm{osc}}^{\mathrm{vel}}$ | $f_{\mathrm{osc}}^{\mathrm{len}}$ | $\Delta E - \Delta E^{\text{def2-QZVPP}}$ [eV] |
| 1 | 0.5945 | 0.0202 | 0.0205 | -0.0048 |
| 2 | 0.6913 | 0.0002 | 0.0003 | 0.0027 |
| 3 | 1.1449 | 0.0015 | 0.0016 | 0.0030 |
| 4 | 1.1879 | 0.0004 | 0.0004 | -0.0035 |
| 5 | 1.5544 | 0.0006 | 0.0006 | -0.0013 |
| MAD | | | | 0.0031 |
| MaxSD | | | | -0.0048 |
| **def2-QZVPP** | | | | |
| # Excitation | $\Delta E$ [eV] | $f_{\mathrm{osc}}^{\mathrm{vel}}$ | $f_{\mathrm{osc}}^{\mathrm{len}}$ | |
| 1 | 0.5993 | 0.0205 | 0.0208 | |
| 2 | 0.6886 | 0.0003 | 0.0003 | |
| 3 | 1.1418 | 0.0016 | 0.0016 | |
| 4 | 1.1914 | 0.0004 | 0.0004 | |
| 5 | 1.5556 | 0.0006 | 0.0006 | |

[a] BLYP35/LANL2DZ(Ru)/6-31G**/COSMO($CH_2Cl_2$) structures. Oscillator strengths are given in the velocity and length representation. Basis set convergence in TDDFT is indicated by the agreement of these representations (as is the case here for def2-QZVPP). MAD and MaxSD are the mean absolute and maximum signed deviations, respectively.

## References


[1] a) M. A. Fox, J. D. Farmer, R. L. Roberts, M. G. Humphrey, P. J. Low, *Organometallics* **2009**, *28*, 5266-5269; b) J. B. G. Gluyas, A. J. Boden, S. G. Eaves, H. Yu, P. J. Low, *Dalton Trans.* **2014**, *43*, 6291-6294.

[2] N. G. Connelly, W. E. Geiger, *Chem. Rev.* **1996**, *96*, 877-910.

[3] M. Krejcik, M. Danek, F. Hartl, *J. Electroanal. Chem.* **1991**, *317*, 179-187.

[4] a) G. Z. Li, S. Azuma, S. Sato, H. Minegishi, H. Nakamura, *Bioorg. Med. Chem. Lett.* **2015**, *25*, 2624-2628; b) F. Jiang, D. I. Trupp, N. Algethami, H. N. Zheng, W. X. He, A. Alqorashi, C. X. Zhu, C. Tang, R. H. Li, J. Y. Liu, H. Sadeghi, J. Shi, R. Davidson, M. Korb, A. N. Sobolev, M. Naher, S. Sangtarash, P. J. Low, W. J. Hong, C. J. Lambert, *Angew. Chem. Int. Ed.* **2019**, *58*, 18987-18993; *Angew. Chem.* **2019**, *131*, 19163 - 19169.

[5] B. A. Boughton, L. Hor, J. A. Gerrard, C. A. Hutton, *Bioorgan. Med. Chem.* **2012**, *20*, 2419-2426.

[6] J. B. G. Gluyas, N. J. Brown, J. D. Farmer, P. J. Low, *Aust. J. Chem.* **2017**, *70*, 113-119.

[7] a) G. M. Sheldrick, *Acta Crystallogr. A* **2015**, *71*, 3-8; b) G. M. Sheldrick, *Acta Crystallogr. C* **2015**, *71*, 3-8.

[8] O. V. Dolomanov, L. J. Bourhis, R. J. Gildea, J. A. K. Howard, H. Puschmann, *J. Appl. Crystallogr.* **2009**, *42*, 339-341.

[9] L. J. Farrugia, *J. Appl. Crystallogr.* **2012**, *45*, 849-854.

[10] A. Thorn, G. M. Sheldrick, *Acta Crystallogr. A* **2008**, *64*, C221-C221.

[11] a) CrysAlisPro 1.171.141.103a Rigaku Oxford Diffraction. 2021. Available online: https://www.rigaku.com/products/crystallography/crysalis; b) CrysAlisPro V1.171.39.46 Rigaku Oxford Diffraction. 2018.

[12] S. G. Balasubramani, G. P. Chen, S. Coriani, M. Diedenhofen, M. S. Frank, Y. J. Franzke, F. Furche, R. Grotjahn, M. E. Harding, C. Hättig, A. Hellweg, B. Helmich-Paris, C. Holzer, U. Huniar, M. Kaupp, A. Marefat Khah, S. Karbalaei Khani, T. Müller, F. Mack, B. D. Nguyen, S. M. Parker, E. Perlt, D. Rappoport, K. Reiter, S. Roy, M. Rückert, G. Schmitz, M. Sierka, E. Tapavicza, D. P. Tew, C. van Wüllen, V. K. Voora, F. Weigend, A. Wodyński, J. M. Yu, *J. Chem. Phys.* **2020**, *152*, 184107.

[13] TURBOMOLE V7.6 2021, a development of University of Karlsruhe and Forschungszentrum Karlsruhe GmbH, 1989-2007, TURBOMOLE GmbH, since 2007; available from http://www.turbomole.org.

[14] M. Haasler, T. M. Maier, R. Grotjahn, S. Gückel, A. V. Arbuznikov, M. Kaupp, *J. Chem. Theory Comput.* **2020**, *16*, 5645-5657.

[15] S. Klawohn, M. Kaupp, A. Karton, *J. Chem. Theory Comput.* **2018**, *14*, 3512-3523.

[16] S. Gückel, P. Safari, S. M. Bagher Hosseini Ghazvini, M. R. Hall, J. B. G. Gluyas, M. Kaupp, P. J. Low, *Organometallics* **2021**, *40*, 346-357.

[17] S. Gückel, J. B. G. Gluyas, S. G. Eaves, P. Safari, D. S. Yufit, A. N. Sobolev, M. Kaupp, P. J. Low, *Chem. Eur. J.* **2019**, *25*, 8837-8853.

[18] M. Renz, K. Theilacker, C. Lambert, M. Kaupp, *J. Am. Chem. Soc.* **2009**, *131*, 16292-16302.

[19] A. P. Scott, L. Radom, *J. Phys. Chem.* **1996**, *100*, 16502-16513.

[20] T. Shimanouchi, in *NIST Chemistry WebBook, NIST Standard Reference Database Number 69* (Ed.: P. J. L. a. W. G. Mallard), National Institute of

Standards and Technology, Gaithersburg MD, 20899, https://doi.org/10.18434/T4D303, retrieved March 15, 2022.
[21] F. Weigend, R. Ahlrichs, *Phys. Chem. Chem. Phys.* **2005**, *7*, 3297-3305.
[22] D. Andrae, U. Häußermann, M. Dolg, H. Stoll, H. Preuß, *Theor. Chim. Acta* **1990**, *77*, 123--141.
[23] F. Weigend, *Phys. Chem. Chem. Phys.* **2006**, *8*, 1057-1065.
[24] S. Grimme, J. Antony, S. Ehrlich, H. Krieg, *J. Chem. Phys.* **2010**, *132*, 154104.
[25] A. D. Becke, E. R. Johnson, *J. Chem. Phys.* **2005**, *123*, 154101.
[26] A. Schäfer, A. Klamt, D. Sattel, J. C. W. Lohrenz, F. Eckert, *Phys. Chem. Chem. Phys.* **2000**, *2*, 2187-2193.